



Cite this: *New J. Chem.*, 2023, 47, 2949

Improving the methane aromatization activity and anti-carbon deposition on MCM-22 through nano α -MoO₃ modification

Jing Hu,^a Chunxue Yang,^a Bing Liu,^a Xinyu Zhao,^a Yin Wang,^a Xiaohui Wang,^a Jinglin Liu^{*a} and Jingqi Guan ^{*b}

Natural gas is considered to be an important energy and hydrocarbon feedstock. To overcome the harmful combustion of natural gas and convert it to high-value-added products, the development of efficient and stable catalysts *via* methane dehydroaromatization (MDA) is needed. Here, we use nano α -MoO₃ to modify the MCM-22 zeolite for MDA, achieving a 13.3% methane conversion and a 9.1% yield of aromatics. Compared with commercial MoO₃, the α -MoO₃ modified MCM-22 possesses more Mo species in the zeolite pores, showing a higher catalytic activity, more MoC_x active sites during MDA, exhibiting a higher benzene selectivity, and fewer Brønsted acid sites, leading to a strong anti-carbon deposition ability.

Received 4th November 2022,
Accepted 5th January 2023

DOI: 10.1039/d2nj05415a

rsc.li/njc

1. Introduction

Methane, the main component of natural gas, shale gas and combustible ice, has the largest hydrogen/carbon ratio and has a greater impact on the greenhouse effect than CO₂. The direct conversion of methane into high-value-added carbon-containing organic compounds and green hydrogen (without generating additional carbon dioxide) is an important means of achieving carbon neutrality. The MDA reaction is one of the most promising routes for the direct conversion of methane to hydrogen.^{1,2} Since Wang *et al.* reported that the Mo/HZSM-5 catalyst showed high selectivity for benzene (>90%) at around 700 °C under atmospheric pressure, researchers have focused on the nature and evolution of active Mo species and the role of zeolite carriers in MDA.^{3,4} However, MDA is a thermodynamically restricted process that requires high reaction temperatures (typically between 600 and 800 °C), to achieve a balance of about 10% methane conversion and up to 80% benzene selectivity.⁵ Moreover, the serious phenomenon of polyaromatic hydrocarbon coking and carbon deposition occurs, resulting in rapid deactivation of the catalysts and therefore limiting the industrial application of MDA. Mo species in the catalyst interact with methane and are converted to molybdenum suboxides or carbide during the induction phase of MDA

which are regarded as the Mo active centre, and then ethylene is generated *via* C–C bond coupling.^{6,7} The strong Brønsted acid sites in the zeolite promote the aromatization of ethylene and the production of benzene and other aromatic hydrocarbons.^{8,9} The distribution of Mo species in the zeolite channels plays a vital role in the catalytic stability and anti-carbon activity of catalysts. The traditional preparation procedure for catalysts is usually *via* the wet impregnation of molybdenum salt on a ZSM-5 support using ammonium heptamolybdate, (NH₄)₆Mo₇O₂₄·4H₂O,¹⁰ or *via* solid-state exchange from physical mixtures of MoO₃ and H-ZSM5 powders,^{11–13} before calcination in air at 550 °C, leading to well-distributed molybdenum oxide species in zeolite channels and small molybdenum oxide aggregates on the zeolite surface. However, the carbon deposition rate and the decrease in the catalyst activity remain high in the MDA process.

Various efforts have been devoted to enhancing the Mo dispersion.^{14–16} Velebna *et al.* prepared Mo/ZSM-5 using ammonium molybdate as the precursor through mechanical mixing, ultrasonic treatment,¹⁷ rotary evaporation and microwave treatment and found that the catalyst prepared *via* the microwave radiation method showed the optimum Mo dispersion, thus showing the best catalytic performance. Julian *et al.*¹⁸ proposed the solvothermal synthesis of the Mo/ZSM-5 catalyst. They utilized supercritical fluids to increase the Mo dispersion, further increasing the number of active centers, as confirmed by XPS, thus showing a higher methane conversion than catalysts obtained using the impregnation method. In addition, Julian *et al.*¹⁹ used polyoxomolybdate (POM) anions as the Mo precursor to prepare MDA catalysts and found that the catalyst

^a College of Chemistry and Materials Science, Key Laboratory of Natural Products Chemistry and Functional Molecular Synthesis, Inner Mongolia Minzu University, Tongliao, 028000, P. R. China. E-mail: jlliu2000@126.com

^b Institute of Physical Chemistry, College of Chemistry, Jilin University, Changchun, 130023, P. R. China. E-mail: guanjq@jlu.edu.cn

modified with an Mo₆ precursor is a promising MDA catalyst. Mishra *et al.*¹⁰ prepared alkaline modified Mo/HZMS-5, which exhibited an excellent catalytic performance due to the addition of secondary mesoporous pores, promoting the distribution of Mo species in the pores and the generation of more active Mo sites. Xu *et al.*²⁰ prepared a hollow HZSM-5 supported MoO₃ catalyst with an enhanced diffusion capacity and an optimized acid content, greatly improving the propane conversion, aromatic selectivity, and catalytic stability. Nam *et al.*²¹ confirmed that NiO modified Mo/HZSM-5 can enhance the dispersion of MoC_x active sites, inhibiting the formation of coke, and improving the catalytic performance.

The high-silica zeolite MCM-22 is composed of three types of pores that are larger than those of ZSM-5, including 10-membered ring (MR) sinusoidal channel (4.1 × 5.1 D), 12-element rings (12 MR) supercages (7.1 × 18.2 D), and external pockets (7.1 × 7.0 D). The unique structure and physicochemical properties make it an ideal catalyst for many reactions, such as alkylation, aromatization and isomerization.²² Here, we explore a facile method to synthesize α-MoO₃ nanoparticles to modify the zeolite MCM-22 to enhance the MDA activity of the catalyst. The α-MoO₃ was obtained by calcining a mixture of ammonium molybdate ((NH₄)₆Mo₇O₂₄·7H₂O) and oxalic acid, which was then used to modify the MCM-22 to prepare Mo/HMCM-22, which exhibits an excellent catalytic performance for the MDA reaction.

2. Experimental

2.1 Preparation of MoO₃(OA)

Ammonium molybdate (3.0897 g) and oxalic acid (1.5759 g) were introduced into an agate mortar and ground to a wet state. Then the mixture was dried at 100 °C, followed by calcination in a muffle furnace at 500 °C for 2 h. The obtained sample was denoted as MoO₃(OA).

2.2 Preparation of Mo-based MCM-22

H-type MCM-22 zeolite (0.8 g) (Kaite New Material Technology Co., Tianjin, China) and commercial MoO₃ or MoO₃(OA) (0.048 g) were ground thoroughly using a mortar before calcination at 550 °C for 5 h to obtain the product of 6 wt% Mo-based MCM-22 zeolite, which are denoted by Mo(C)-HMCM-22 and Mo(OA)-HMCM-22, respectively.

2.3 Catalyst characterization

X-Ray diffraction (XRD) characterization was performed using a Smart Lab X-ray diffractometer using Cu Kα radiation. The morphology and particle size of the samples were obtained using an FESEM XL-30 field emission scanning electron microscope (SEM). Transmission electron microscopy (TEM) and energy-dispersive spectroscopy (EDS) measurements were obtained using FEI S/TEM Talos F200S equipment at 200 kV. The specific surface area of the catalyst was determined *via* the N₂ adsorption-desorption method at -196 °C using Micromeritics ASAP 2020 apparatus, and the sample was outgassed under

vacuum at 300 °C for 5 h prior to the analysis. The pore size distributions were determined using non-local density functional theory (NLDFT). The FT-IR spectrum of the catalyst was obtained using a Shimadzu Lab Total spectrophotometer. Thermally programmed reduction (TPR) analysis was carried out using an AutoChem 2720 instrument. The acidity of the catalyst was tested *via* NH₃-TPD using an Auto Chem 2720 instrument. X-Ray photoelectron spectroscopy (XPS) was carried out using an ESCALAB 250Xi analyzer. Thermogravimetric analysis was analyzed using a Shimadzu DTG-60 instrument. The infrared (FTIR) spectroscopy of adsorbed pyridine was conducted to evaluate the acidity of the samples. Samples were pressed to self-supporting discs (30 mg, diameter 1.3 cm) and then outgassed *in situ* under vacuum at 400 °C for 1 h to remove adsorbed species. Pyridine was adsorbed on the outgassed samples at 200 °C for 30 min, and then the FTIR spectra were recorded at 200 °C. UV-vis DRS spectra were recorded using a Shimadzu UV-3600 spectrometer using BaSO₄ as the standard at room temperature.

2.4 Catalytic tests

The evaluation of the catalyst was carried out using a continuous-flow fixed-bed reactor. The inner diameter of the medium quartz reaction tube was 10 mm, the catalyst loading was 0.5 g, the space velocity was 1500 mL (g h)⁻¹, the CH₄ flow rate was 14.2 mL min⁻¹ and the pressure was 0.1 MPa. The catalyst was first heated to 700 °C in a N₂ atmosphere and activated at this temperature for 30 min before switching to a 7.5% N₂-92.5% CH₄ feed gas. The reaction product was analysed *via* on-line analysis using a Tianmei SCION gas chromatograph equipped with thermal conductivity detectors (TCD) and flame ionization detectors (FID). The products were calculated *via* the carbon balance analysis method using N₂ as an internal standard.²³

The specific calculation formula are as follows:

$$F^{\text{in}} A_{\text{N}_2}^{\text{in}} = F^{\text{out}} A_{\text{N}_2}^{\text{out}}$$

$$\text{Methane conversion (\%)} = \frac{F^{\text{in}} X_{\text{methane}}^{\text{in}} - F^{\text{out}} X_{\text{methane}}^{\text{out}}}{F^{\text{in}} X_{\text{methane}}^{\text{in}}}$$

$$S_{\text{product}}^{\text{carbon}} (\%) = \frac{F^{\text{out}} X_{\text{product}}^{\text{out}} N_{\text{product}}^{\text{carbon}}}{F^{\text{in}} X_{\text{methane}}^{\text{in}} - F^{\text{out}} X_{\text{methane}}^{\text{out}}}$$

$$S_{\text{coke}} (\%) = 1 - \sum_{\text{product}}^S \text{carbon}$$

The total gas flow rate, mole fraction and carbon number in a molecule are denoted as F , X and N^{carbon} , respectively.

3. Results and discussion

3.1 Structural analysis

To determine the composition of α-MoO₃ and Mo(OA)-HMCM-22 and their crystal phase structures, the samples were tested using XRD (Fig. 1). Fig. 1a reveals peaks located at 12.9°, 23.4°,

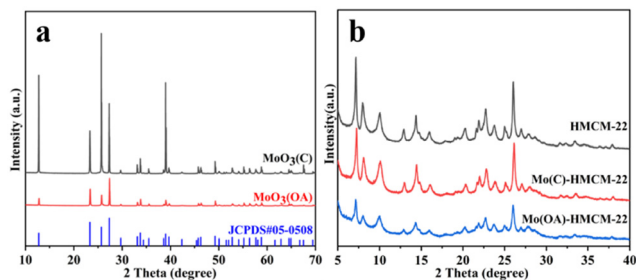


Fig. 1 XRD patterns of (a) $\text{MoO}_3(\text{C})$, $\text{MoO}_3(\text{OA})$ and orthorhombic-phase MoO_3 , and (b) HMCM-22, Mo(C)-HMCM-22 and Mo(OA)-HMCM-22.

25.9° , 27.4° and 39.1° , which are assigned to the (020), (110), (040), (021) and (060) crystal planes, respectively. Compared with the standard card of orthorhombic-phase MoO_3 (JCPDS No. 05-0508), there are no additional peaks, indicating that the target product of orthorhombic α - MoO_3 obtained by the solid-phase chemical reaction between oxalic acid and ammonium molybdate is pure. Fig. 1b shows the XRD patterns of HMCM-22, Mo(C)-HMCM-22 and Mo(OA)-HMCM-22. The 2θ peaks at 7.1° , 7.9° , 10.0° , 25.0° and 26.0° correspond to the (100), (101), (102), (220) and (310) planes, respectively,²⁴ which belong to the typical MCM-22 structure. Compared with HMCM-22, the crystallinity of the Mo-supported catalysts decreases, the crystallinity of the nano- MoO_3 modified MCM-22 catalyst (Mo(OA)-HMCM-22) decreases more significantly than that of the commercial MoO_3 modified MCM-22, and the diffraction peaks of the MoO_3 crystals completely disappear in the Mo(OA)-HMCM-22 catalyst, demonstrating the good dispersion of Mo species.

Fig. 2 shows the SEM images of commercial MoO_3 and $\text{MoO}_3(\text{OA})$. The $\text{MoO}_3(\text{OA})$ particles are distributed in the range

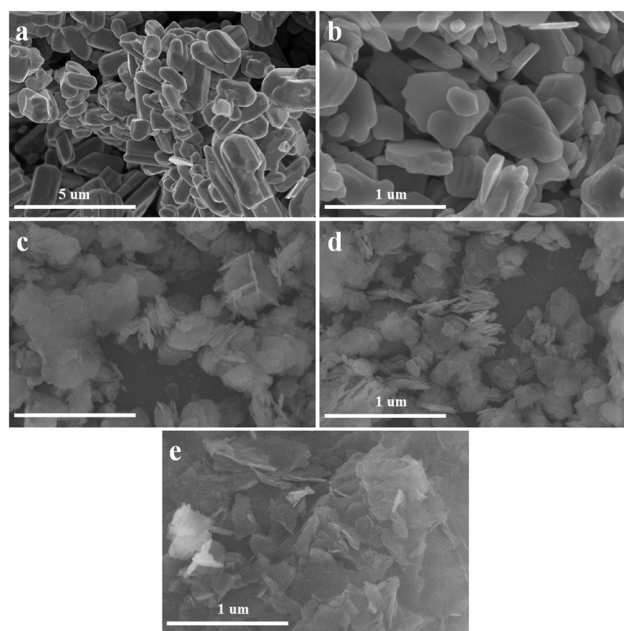


Fig. 2 SEM images of (a) commercial MoO_3 , (b) $\text{MoO}_3(\text{OA})$, (c) Mo(C)-HMCM-22, (d) Mo(OA)-HMCM-22 and (e) HMCM-22.

of 120–460 nm (Fig. 2b), which are much smaller than commercial MoO_3 (0.7–2.1 μm ; Fig. 2a). The SEM images of HMCM-22 and HMCM-22 after the loading of different modified MoO_3 are shown in Fig. 2c–e. The catalysts are flake-like crystals with a regular shape,^{25,26} denoting that the introduction of Mo species to the zeolite under calcination does not affect the morphology of the MCM-22 crystal. EDS analysis was performed to notarize the distribution of Mo species in the catalyst (Fig. 3), exhibiting that the Si, O, Al and Mo elements are uniformly distributed in the HMCM-22 zeolite.

FT-IR spectroscopy was carried out to analyze the skeleton structure of HMCM-22, Mo(C)-HMCM-22 and Mo(OA)-HMCM-22. As displayed in Fig. 4a, the absorption peak at 1242 cm^{-1} is attributed to the asymmetric stretching vibration of the Si(Al) tetrahedron in the HMCM-22 zeolite. The absorption peak in the region with a frequency greater than 3000 cm^{-1} is ascribed to the stretching vibration peak of the hydroxyl group. The peaks at 1242 cm^{-1} and 1098 cm^{-1} are due to the T–O (T = Si and Al) asymmetric stretching vibration, and the peak at 804 cm^{-1} is attributed to the T–O symmetric stretching vibration. The absorption peak at 451 cm^{-1} is caused by the bending vibration of the internal tetrahedron T–O,²⁷ while the peaks at 600 cm^{-1} and 550 cm^{-1} are ascribed to the tetrahedral double ring vibration in the zeolite framework, which are typical characteristics of microporous zeolites.²⁸ After the loading of

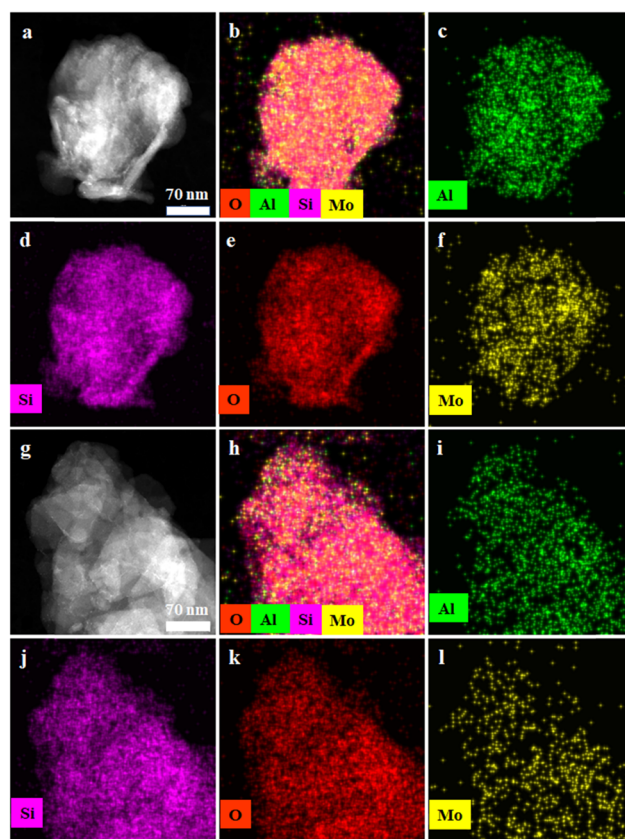


Fig. 3 TEM images and STEM-EDS elemental maps of Mo(OA)-HMCM-22 (a–f) and Mo(C)-HMCM-22 (g–l).

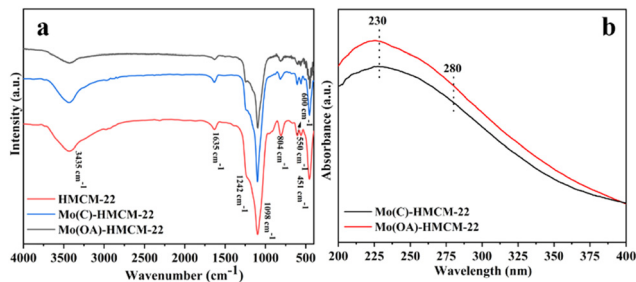


Fig. 4 FT-IR spectra (a) and UV-vis DRS spectra (b) of the catalysts.

Mo species, the peak intensity of each characteristic absorption peak decreases significantly, and the decreased intensity of Mo(OA)-HMCM-22 is more significant than that of Mo(C)-HMCM-22, indicating that more Mo species combine with -OH in the skeleton, thereby reducing the intensity.

The interaction between the Mo oxide and the HMCM-22 carrier was evaluated using UV-vis DRS spectroscopy (Fig. 4b). The Mo-oxo species have strong absorption bands in the 200–400 nm wavelength range, which are attributed to ligand-to-metal charge transfer (LMCT) from the O (2p) to the Mo (3d) orbital. It is reported that LMCT bands of 210–250 nm and 280 nm due to Mo species binding to the acid sites (Mo–O–Al) or Mo-oxo located in tetrahedral coordination environments (MoO₄). In addition, Mo-oxo centers in octahedral environments (MoO₆) or Mo nanoparticles have been observed at higher wavelengths (300–330 nm). All of these absorption characteristics confirm the formation of MoO_x species in different coordination environments and with different symmetries.¹⁰ It can be seen from Fig. 4b that the UV-Vis spectra of both catalysts exhibit absorption bands at 230 nm, suggesting that most Mo-oxo species are well adsorbed to the Al–O–Si site of HMCM-22 in an isolated tetrahedral structure (MoO₄).²⁹ In addition, Mo(OA)-HMCM-22 shows the strongest band at 230 nm, indicating the presence of more MoO₄ or Mo interacting with the acid sites.

Fig. 5 shows the nitrogen adsorption–desorption curves and pore size distributions of HMCM-22, Mo(C)-HMCM-22 and Mo(OA)-HMCM-22. All the three materials exhibit type I isotherms in the low relative pressure region, which confirms their microporous nature.³⁰ The adsorption isotherms show a trend of rapid increase and clear hysteresis rings appear at the relative pressure of $P/P_0 > 0.8$, which may be caused by capillary condensation of the mesopores, indicating that the MCM-22 materials contain a certain amount of mesopores. Table 1 exhibits that the specific surface areas of HMCM-22, Mo(C)-HMCM-22 and Mo(OA)-HMCM-22 are 496 cm² g⁻¹, 357 cm² g⁻¹ and 308 cm² g⁻¹, respectively. The pore size of zeolite that well retained after loading of the Mo species. The micropore volume of the catalyst supported by Mo species is reduced significantly, and the decreased degree of Mo(OA)-HMCM-22 is greater than that of Mo(C)-HMCM-22. Compared with the HMCM-22 zeolite, the micropore volume of Mo(OA)-HMCM-22 decreases to 64.2% because the α -MoO₃ species exhibit a higher dispersity in the MCM-22 channels and

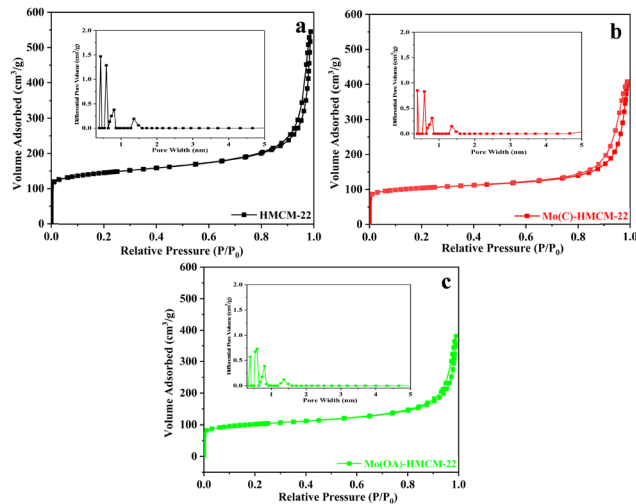


Fig. 5 N₂-adsorption-desorption and pore size distribution (inset) for (a) HMCM-22, (b) Mo(C)-HMCM-22 and (c) Mo(OA)-HMCM-22.

Table 1 Textural properties of HMCM-22, Mo(C)-HMCM-22 and Mo(OA)-HMCM-22

Sample	S_{BET}^a	$S_{\text{micropore}}^b$ (m ² g ⁻¹)	S_{external}^b (m ² g ⁻¹)	$V_{\text{micropore}}^b$ (cm ³ g ⁻¹)	V_{total}^c (cm ³ g ⁻¹)
HMCM-22	496	309	187	0.14	0.85
Mo(C)-HMCM-22	352	233	119	0.11	0.67
Mo(OA)-HMCM-22	345	208	136	0.09	0.65

^a Calculated using the BET method. ^b Calculated using the *t*-plot method. ^c Calculated with the adsorption capacity at P/P_0 of 0.98.

combine with Si–OH or Al–OH in the zeolite at high temperature, resulting in a reduction of the specific surface area and pore volume.

It has been reported that active MoC_x species are more likely to be immobilized on the framework Al sites. Therefore, the formation of MoC_x species could be deduced by measuring the number of acid sites. When the anchored MoC_x in the zeolite pores increases, more anchor sites are occupied on the framework Al, leading to a decrease in the acid content.²¹ In this study, NH₃-TPD was performed to investigate the acidity of the catalyst. From Fig. 6a, HMCM-22 shows three classic peaks after the curve is fitted. The high temperature desorption peak (peak H) of the NH₃-TPD profiles corresponds to the silicon and aluminum bridging hydroxyl Brønsted acid site (–Al_F–O(H)–Si_F–), which is attributed to the exchange of Mo species with Brønsted acid sites in the MCM-22 zeolite. The low-temperature desorption peak (peak L) is caused by the combination of NH₃ with a weak acid, while the moderate-temperature desorption peak (peak M) is attributed to the exchangeable protonic sites binding with NH₃. The NH₃ consumption by the HMCM-22, Mo(C)-HMCM-22 and Mo(OA)-HMCM-22 catalysts at various temperatures is summarized in Table 2. It is shown that the order of total NH₃ consumption of the three catalysts follows the order HMCM-22 (39 μmol g⁻¹) > Mo(C)-HMCM-22 (37 μmol g⁻¹) > Mo(OA)-HMCM-22 (34 μmol g⁻¹).

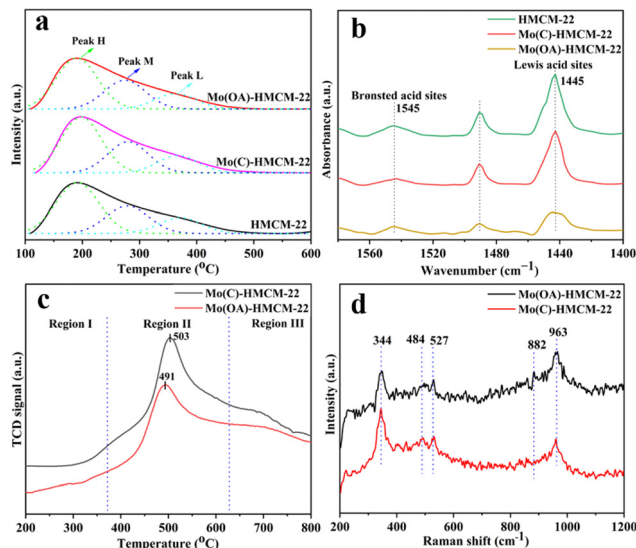


Fig. 6 (a) NH_3 -TPD profiles of HMCM-22, Mo(C)-HMCM-22 and Mo(OA)-HMCM-22, and (b) IR spectra of pyridine adsorbed on HMCM-22, Mo(C)-HMCM-22 and Mo(OA)-HMCM-22; (c) H_2 -TPR profiles and (d) Raman spectra of Mo(C)-HMCM-22 and Mo(OA)-HMCM-22.

Table 2 NH_3 consumption for HMCM-22, Mo(C)-HMCM-22 and Mo(OA)-HMCM-22

Sample	Temperature (°C)			NH_3 consumption ($\mu\text{mol g}^{-1}$)			Total ($\mu\text{mol g}^{-1}$)
	Peak L	Peak M	Peak H	Peak L	Peak M	Peak H	
HMCM-22	191	278	371	20.8	11.6	6.6	39
Mo(C)-HMCM-22	198	280	367	20.0	10.9	6.1	37
Mo(OA)-HMCM-22	190	274	362	18.4	10.1	5.5	34

These results show that $\alpha\text{-MoO}_3$ is more likely to migrate to the pores and framework of the zeolite and thus reduce the acidity of the catalyst. Since excess Brønsted acid sites can exacerbate the formation of carbon deposits, resulting in a lower catalytic performance, it can be inferred from the NH_3 -TPD profiles that the Mo(OA)-HMCM-22 catalyst has a better methane aromatization performance.

The FTIR-pyridine spectra after the desorption of pyridine at 200 °C exhibit many acid sites for HMCM-22 and Mo-modified HMCM-22 (Table 3). From Fig. 6b, the spectral bands of 1545 cm^{-1} and 1455 cm^{-1} are attributed to the Brønsted and Lewis acid sites, respectively, and the medium band located at 1490 cm^{-1} is ascribed to the co-contribution of pyridine adsorbed on the Lewis and Brønsted acid sites.³¹ The acidity of the HMCM-22 zeolite modified by Mo species is dramatically reduced. Moreover, the acidity of the Mo(OA)-HMCM-22 catalyst decreases to a greater extent than the Mo(C)-HMCM-22 catalyst, indicating that MoO_x sublimes and diffuses to the HMCM-22 zeolite, which is consistent with the NH_3 -TPD results.

H_2 -TPR studies were performed to gain a deeper understanding of the reduction of Mo species on HMCM-22. The H_2 -TPR profile can be divided into three temperature regions.

Table 3 Quantitative results from pyridine-FTIR of HMCM-22, Mo(C)-HMCM-22 and Mo(OA)-HMCM-22

Sample	Brønsted acid ($\mu\text{mol g}^{-1}$)	Lewis acid ($\mu\text{mol g}^{-1}$)	$B_{\text{acid}}/L_{\text{acid}}$
HMCM-22	29.0287	88.5736	0.3277
Mo(C)-HMCM-22	18.0744	77.2283	0.2340
Mo(OA)-HMCM-22	16.0041	71.0388	0.2253

Region I (200–400 °C) is attributed to the reduction of the amorphous polymer molybdate. Region II, between 400 and 700 °C, corresponds to the reduction of octahedral MoO_3 to tetrahedral synergistic MoO_2 , which is regarded as the primary reduction feature,¹⁰ while region III above 700 °C is ascribed to the complete reduction of MoO_2 to metallic Mo species. As can be seen in Fig. 6c, the reduction characteristics of both catalysts are different in region II. The reducibility of MoO_3 to MoO_2 in the Mo(OA)-HMCM-22 catalyst decreases, which is because the anchoring mode of the MoO_3 species in the HMCM-22 channels has changed after $\alpha\text{-MoO}_3$ modification. The lower reducibility observed in Mo(OA)-HMCM-22 is caused by the strong combination of MoO_x species with the HMCM-22 zeolite. The NH_3 -TPD studies confirm that Mo(OA)-HMCM-22 has a lower Brønsted acid site concentration due to more MoO_x species migrating into the channels of the HMCM-22 zeolite. The reduction temperature decreases from 503 °C for Mo(C)-HMCM-22 to 491 °C for Mo(OA)-HMCM-22, indicating that the interaction of Mo oxo species with the zeolite surface could be improved for nano $\alpha\text{-MoO}_3$ -modified HMCM-22.³²

Raman spectra were obtained to analyse the chemical bonding of MoO_x species in the MCM-22 channels. As shown in Fig. 6d, the bands located at 344, 484, 527 cm^{-1} are assigned to the MCM-22 characteristic framework.²⁶ Mo(OA)-HMCM-22 catalyst has a wider scattering at around 850 cm^{-1} compared with the Mo(C)-HMCM-22 catalyst, showing that more poly-oxomolybdate phases are formed. The occurrence of the 960–975 cm^{-1} band is ascribed to the existence of hydrated monomeric supported MoO_x species, indicating the $\nu(\text{Mo}=\text{O})$ stretching vibration.³³ These results indicate that molybdenum oxide is well associated with different Al sites within the MCM-22 zeolite modified with nano $\alpha\text{-MoO}_3$.

3.2 MDA testing

The MDA performance on Mo(C)-HMCM-22 and Mo(OA)-HMCM-22 is shown in Fig. 7 and Table 4, proving the conversion of methane and the yield of aromatics within 480 min. As displayed in Fig. 7a, both catalysts show a low methane conversion at an early stage due to methane being activated to form MoO_xC_y and MoC_x at 700 °C during the induction period.^{10,34} A maximum yield of aromatics with the time on stream is revealed for Mo(OA)-HMCM-22 and Mo(C)-HMCM-22 (Fig. 7b), and is then reduced as the reaction proceeds.^{35,36} Compared with Mo(C)-HMCM-22, methane conversion is higher on the Mo(OA)-HMCM-22 with time on stream, demonstrating its higher catalytic activity. In addition, the conversion

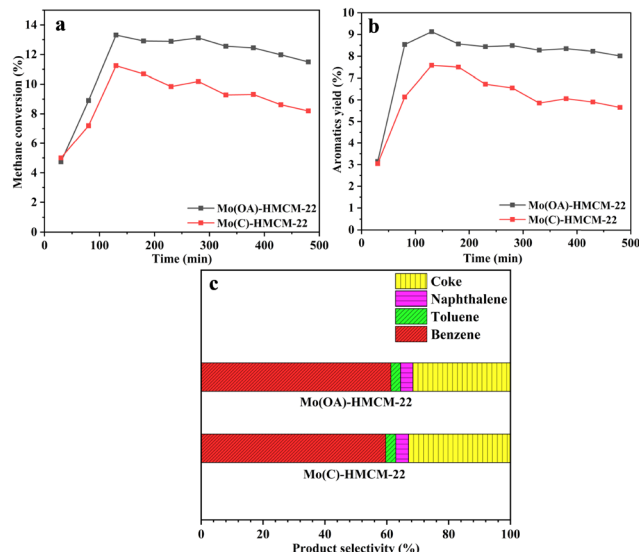


Fig. 7 (a) Methane conversion, (b) aromatics yield and (c) product selectivity.

of methane gradually reduces with the time on stream, which may be assigned to slow catalyst deactivation due to carbonaceous deposition, thus reducing the catalytic activity.^{38,39} As shown in Table 4, Mo(OA)-HMCM-22 has its highest aromatics yield (9.1%) at around 130 min, which is superior to Mo(C)-HMCM-22 (7.5%). Notably, Mo(OA)-HMCM-22 exhibits a higher methane conversion (13.3%) than that of Mo(C)-HMCM-22 (11.2%), which may be due to a better distribution of Mo in the catalyst and the generation of more active Mo sites in the former.^{40,41} In addition, Mo(OA)-HMCM-22 shows a higher TOF value than Mo(C)-HMCM-22 (14.9 h^{-1} vs. 13.3 h^{-1}) at 130 min. According to the results of EDS mapping, FT-IR and Raman spectroscopy, and NH_3 -TPD, the enhanced activity of the Mo(OA)-HMCM-22 catalyst is mainly attributed to there being more Mo species inside the channels of HMCM-22 associated with Brønsted acid sites, thus moderately reducing the density of acid centres and enhancing the overall accessibility of the acid centres.^{33,42}

The selectivity for different products is exhibited in Fig. 7c and Table 4. The selectivity for benzene over Mo(OA)-HMCM-22 is 61.3%, which is higher than that of the Mo(C)-HMCM-22 catalyst (59.6%). Moreover, the selectivity for coke over Mo(OA)-MCM-22 after 480 min is slightly lower than that of

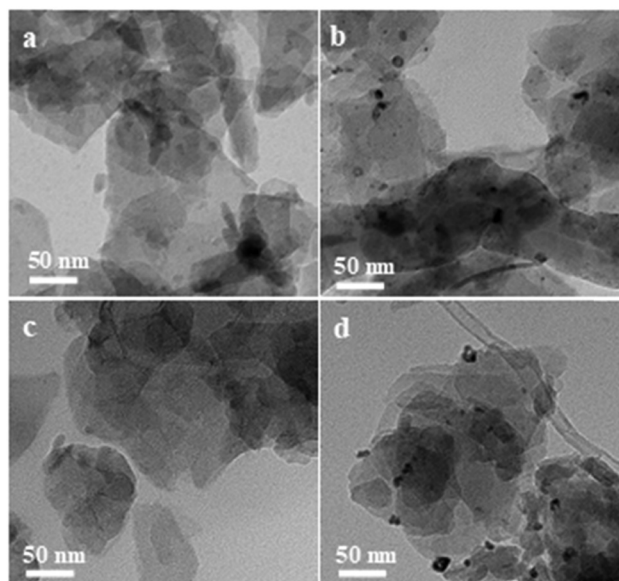


Fig. 8 TEM images of (a) fresh Mo(C)-HMCM-22, (b) used Mo(C)-HMCM-22, (c) fresh Mo(OA)-HMCM-22, and (d) used Mo(OA)-HMCM-22.

Mo(C)-MCM-22 (30.5% vs. 31.9%, respectively). It is demonstrated that HMCM-22 modified with $\alpha\text{-MoO}_3$ has a positive effect on enhancing the catalytic performance. Since Brønsted acid centres are conducive to the formation of carbon deposits,^{11,43} Mo(OA)-HMCM-22 exhibits small Brønsted acid sites, leading to good stability in the MDA reaction.

The surface characteristics of post-reaction catalysts change greatly due to the creation of metal carbides and the deposition of carbon. In this sense, significant coke deposition as well as sintering and separation of Mo species from the zeolite structure are responsible for catalyst deactivation.^{18,44} From TEM images obtained (Fig. 8), both samples show distinct carbide clusters (MoC_x) after the reaction, which are formed during the MDA reaction.

XPS analysis of the fresh and spent catalysts was performed to elaborate the chemical nature of the Mo species. The methane atmosphere promotes the stepwise change in the oxidation state of Mo species, and the Mo oxides are transformed into oxide carbides (MoO_xC_y) and carbide phases (MoC_x) at 700°C .^{44,45} The Mo 3d XPS spectra for the catalysts exhibit two bands for the fresh catalyst, whereas the XPS spectra of the post-reaction catalysts can be fitted to four peaks

Table 4 MDA catalytic results on different catalysts

Catalyst	Mo content ^a (%)	Reaction time (min)	Conversion of CH_4 (%)	TOF (h^{-1})	Selectivity (%)				Yield of aromatics (%)
					Benzene	Toluene	Naphthalene	Coke	
Mo(C)-HMCM-22	5.5	130	11.2	13.3	59.6	3.3	4.1	33.0	7.5
		480	8.2	9.5	61.0	3.1	4.0	31.9	5.6
Mo(OA)-HMCM-22	5.8	130	13.3	14.9	61.3	3.1	4.0	31.6	9.1
		480	11.5	12.9	62.4	3.2	3.9	30.5	8.0
HMCM-22 ³⁷	—	150	0.5	—	—	—	—	≈ 80	—

^a Based on inductively coupled plasma results.

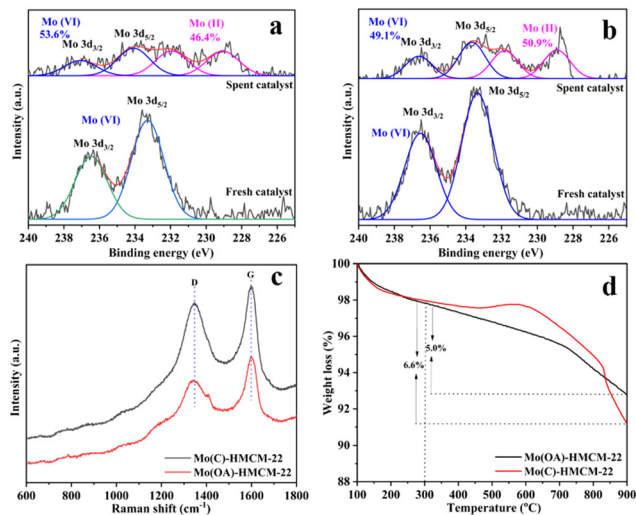


Fig. 9 (a) Mo 3d XPS spectra for fresh and used Mo(C)-HMCM-22. (b) Mo 3d XPS spectra for fresh and used Mo(OA)-HMCM-22. (c) Raman spectra of used Mo(C)-HMCM-22 and Mo(OA)-HMCM-22. (d) Thermogravimetric analysis of used Mo(C)-HMCM-22 and Mo(OA)-HMCM-22.

(Fig. 9a and b). Mo 3d_{3/2} and Mo 3d_{5/2} at binding energy values of 236.6 eV and 233.4 eV, respectively, indicate the presence of Mo in the hexavalent state, while the binding energy values at 228.9 eV and 231.9 eV are due to the formation of molybdenum carbide species (Mo₂C), which are regarded as the active site Mo(II) species that benefit methane activation and the dimerization of CH_x intermediates during the MDA reaction.¹ It is calculated that 50.9% (Mo(II)) and 49.1% (Mo⁶⁺) exist in the used Mo(OA)-HMCM-22, while 46.4% (Mo(II)) and 53.6% (Mo⁶⁺) exist in the used Mo(C)-HMCM-22. Specifically, the proportion of Mo₂C species in the used Mo(OA)-HMCM-22 is clearly higher than that in the used Mo(C)-HMCM-22 because of the effective anchoring of Mo species at Brønsted acid sites in Mo(OA)-HMCM-22.⁴⁶ Therefore, Mo(OA)-HMCM-22 shows a better catalytic performance.

Raman analysis was used to gain a deeper insight into the types and the amount of carbonaceous species on the surface of Mo(C)-HMCM-22 and Mo(OA)-HMCM-22 after 480 min of reaction. As exhibited in Fig. 9c, the Raman spectra of the catalysts exhibit two bands. The G-band located at 1596 cm⁻¹ is generated by the stretching motion of all sp² atom pairs in the carbon ring or long chain, which is ascribed to the ordered graphitic structure. The formation of the D-band (1350 cm⁻¹) is assigned to the presence of disordered aromatics or structurally disordered graphitic species.³⁹ The value of I_D/I_G reflects the disorder degree of the surface carbon species. The I_D/I_G value for Mo(C)-HMCM-22 is 2.88, which is higher than that of Mo(OA)-HMCM-22 (0.85), showing that Mo(C)-HMCM-22 has the more disordered nature of surface graphite-like coke.^{21,47} It is well known that the coke species are generated through MoC_x and amorphous coke, which lead to deactivation of the catalyst. Hence, the result indicates that α-MoO₃-modified HMCM-22 could inhibit the formation of carbon deposits and thus improve the catalytic stability.

The principle of catalyst deactivation can be investigated *via* thermogravimetric analysis of the used samples (Fig. 9d). The first weight loss below 220 °C corresponds to the evaporation of physically and chemically sorbed water. The weight loss above 350 °C is ascribed to the decomposition of metal carbides and coke deposition.¹² The weight loss in this temperature range is 6.6% and 5.0% for Mo(C)-HMCM-22 and Mo(OA)-HMCM-22, respectively. Therefore, it is inferred that more anti-carbon deposition is generated in the α-MoO₃-modified HMCM-22, showing a better catalytic stability in the MDA reaction.

4. Conclusions

We have prepared nano α-MoO₃-modified HMCM-22 for the MDA reaction, where Mo species are highly dispersed into the zeolite, as clarified through various characteristics. Compared with commercial MoO₃, more Mo species can be migrated into the zeolite pores using nano α-MoO₃ modification, thus showing a higher catalytic activity. During the MDA reaction, more MoC_x active sites were generated in Mo(OA)-HMCM-22, thus exhibiting a higher benzene selectivity. In addition, fewer Brønsted acid sites present in Mo(OA)-HMCM-22 lead to its strong anti-carbon deposition ability.

Conflicts of interest

The authors have no conflicts of interest to declare.

Acknowledgements

This research was funded by the Inner Mongolia Natural Science Foundation (2022MS02015, 2017BS0205), the Inner Mongolia Autonomous Region Funding Project for Science & Technology Achievement Transformation (2022YFDZ0039), the Doctoral Scientific Research Foundation of Inner Mongolia Minzu University (BS379, BS431) and the Scientific Research Projects of the Inner Mongolian Higher Educational System (NJZY21418).

Notes and references

- H. W. Ryu, K. Nam, Y. H. Lim and D. H. Kim, *Catal. Today*, 2022, DOI: [10.1016/j.cattod.2022.08.017](https://doi.org/10.1016/j.cattod.2022.08.017).
- D. Kiani, S. Sourav, Y. Tang, J. Baltrusaitis and I. E. Wachs, *Chem. Soc. Rev.*, 2021, **50**, 1251–1268.
- L. Wang, L. Tao, M. Xie, G. Xu, J. Huang and Y. Xu, *Catal. Lett.*, 1993, **21**, 35–41.
- Y. Zhang and H. Jiang, *Chem. Commun.*, 2018, **54**, 10343–10346.
- N. Kosinov and E. J. M. Hensen, *Adv. Mater.*, 2020, **32**, 2002565.
- J. J. Spivey and G. Hutchings, *Chem. Soc. Rev.*, 2014, **43**, 792–803.
- L. Liu, N. Wang, C. Zhu, X. Liu, Y. Zhu, P. Guo, L. Alfilfil, X. Dong, D. Zhang and Y. Han, *Angew. Chem., Int. Ed.*, 2020, **59**, 819–825.

- 8 A. López-Martín, M. F. Sini, M. G. Cutrufello, A. Caballero and G. Colón, *Appl. Catal., B*, 2022, **304**, 120960.
- 9 T. S. Khan, S. Balyan, S. Mishra, K. K. Pant and M. A. Haider, *J. Phys. Chem. C*, 2018, **122**, 1–36.
- 10 D. Mishra, S. Mishra, A. Modak, K. K. Pant and X. S. Zhao, *Fuel Process. Technol.*, 2022, **235**, 107387.
- 11 N. K. Razdan and A. Bhan, *J. Catal.*, 2020, **389**, 667–676.
- 12 C. H. L. Tempelman, V. O. de Rodrigues, E. R. H. van Eck, P. C. M. M. Magusin and E. J. M. Hensen, *Microporous Mesoporous Mater.*, 2015, **203**, 259–273.
- 13 W. Li, G. D. Meitzner, R. W. Borry and E. Iglesia, *J. Catal.*, 2000, **191**, 373–383.
- 14 I. Vollmer, I. Yarulina, F. Kapteijn and J. Gascon, *Chem-CatChem*, 2019, **11**, 39–52.
- 15 V. Ramasubramanian, H. Ramsurn and G. L. Price, *J. Energy Chem.*, 2019, **34**, 20–32.
- 16 A. Galadima and O. Muraza, *Catal. Surv. Asia*, 2019, **23**, 149–170.
- 17 K. Velebna, M. Hornacek, V. Jorik, P. Hudec, M. Caplovicova and L. U. Caplovic, *Microporous Mesoporous Mater.*, 2015, **212**, 146–155.
- 18 I. Julian, M. B. Roedern, J. L. Hueso, S. Irusta, A. K. Baden, R. Mallada, Z. Davis and J. Santamaria, *Appl. Catal., B*, 2020, **263**, 118360.
- 19 I. Julian, J. L. Hueso, N. Lara, A. Solé-Daurá, J. M. Poblet, S. G. Mitchell, R. Mallada and J. Santamaria, *Catal. Sci. Technol.*, 2019, **9**, 5927–5942.
- 20 G. Xu, P. Zhang, J. Cheng, T. Wei, X. Zhu and F. Yang, *J. Solid State Chem.*, 2021, **300**, 122238.
- 21 K. Nam, H. W. Ryu, M. Y. Gim and D. H. Kim, *Appl. Catal., B*, 2021, **296**, 120377.
- 22 L. L. Silva, M. J. Stellato, M. V. Rodrigues, B. J. Hare, J. C. Kerwin, A. S. Bommarius, L. Martins and C. Sievers, *J. Catal.*, 2022, **411**, 187–192.
- 23 S. Liu, Q. Dong, R. Ohnishi and M. Ichikawa, *Chem. Commun.*, 1997, 1455–1456.
- 24 X.-L. Wei, W.-Y. Pan, X. Li, M. Pan, C.-F. Huo, R. Yang and Z.-S. Chao, *Chem. Mater.*, 2020, **32**, 333–340.
- 25 A. Sachse, T. Aumond, J. Rousseau and I. Batonneau-Gener, *Adv. Mater. Interfaces*, 2021, **8**, 2100356.
- 26 T. H. Lim, K. Nam, I. K. Song, K.-Y. Lee and D. H. Kim, *Appl. Catal., A*, 2018, **552**, 11–20.
- 27 P. Sahu, T. V. Haripriya, A. Sreenavya, G. V. Shanbhag, A. Augustin and A. Sakthivel, *J. Chem. Sci.*, 2020, **132**, 153.
- 28 P. Sahu, A. Tincy, A. Sreenavya, G. Shanbhag and A. Sakthivel, *Catal. Lett.*, 2021, **151**, 1336–1349.
- 29 P. Tan, *Appl. Catal., A*, 2019, **580**, 111–120.
- 30 S. Anderson, V. R. Jhonny, S. Karim, D. Urbano, C. Avelino and P. J. A. O. Sibebe, *ACS Omega*, 2018, **3**, 6217–6223.
- 31 J. Chen, T. Liang, J. Li, S. Wang, Z. Qin, P. Wang, L. Huang, W. Fan and J. J. A. C. Wang, *ACS Catal.*, 2016, **6**, 2299–2313.
- 32 S. Mishra, M. Ali Haider and K. K. Pant, *Catal. Lett.*, 2020, **150**, 3653–3666.
- 33 A. Beuque, H. Hu, E. Berrier, A. Sachse, J.-F. Paul and L. Pinard, *Catal. Today*, 2022, **405–406**, 168–181.
- 34 J. Hu, S. Wu, Z. Li, L. Peng, X. Fu, X. Wang, J. Guan and Q. Kan, *Appl. Organomet. Chem.*, 2015, **29**, 638–645.
- 35 R. Simancas, A. Chokkalingam, S. Elangovan, Z. Liu, T. Sano, K. Iyoki, T. Wakihara and T. Okubo, *Chem. Sci.*, 2021, **12**, 7677–7695.
- 36 P. Tan, *Catal. Commun.*, 2018, **103**, 101–104.
- 37 D. Ma, D. Z. Wang, L. L. Su, Y. Y. Shu, Y. Xu and X. H. Bao, *J. Catal.*, 2002, **208**, 260–269.
- 38 Y. Liu, H. Zhang, A. S. G. Wijpkema, F. J. A. G. Coumans, L. Meng, E. A. Uslamin, A. Longo, E. J. M. Hensen and N. Kosinov, *Chem. – Eur. J.*, 2021, **27**, 1–13.
- 39 M. Agote-Arán, R. E. Fletcher, M. Briceno, A. B. Kroner, I. V. Sazanovich, B. Slater, M. E. Rivas, A. W. J. Smith, P. Collier, I. Lezcano-González and A. M. Beale, *Chem-CatChem*, 2020, **12**, 294–304.
- 40 K. Wang, X. Huang and D. Li, *Appl. Catal., A*, 2018, **556**, 10–19.
- 41 W. Gao, G. Qi, Q. Wang, W. Wang, S. Li, I. Hung, Z. Gan, J. Xu and F. Deng, *Angew. Chem., Int. Ed.*, 2021, **60**, 10709–10715.
- 42 N. Rajiv Chandar, S. Agilan, R. Thangarasu, N. Muthukumarasamy, J. Chandrasekaran, S. Arunachalam and S. R. Akshaya, *J. Sol-Gel Sci. Technol.*, 2021, **100**, 451–465.
- 43 M. Rahman, A. Infantes-Molina, A. Boubnov, S. R. Bare and S. J. Khatib, *J. Catal.*, 2019, **375**, 314–328.
- 44 Á. López-Martín, A. Caballero and G. Colón, *Appl. Catal., B*, 2022, **312**, 121382.
- 45 M. Rahman, A. Sridhar and S. J. Khatib, *Appl. Catal., A*, 2018, **558**, 67–80.
- 46 J. Gao, Y. Zheng, J.-M. Jehng, Y. Tang, I. E. Wachs and S. G. Podkolzin, *Science*, 2015, **348**, 686–690.
- 47 Y. Zheng, Y. Tang, J. R. Gallagher, J. Gao, J. T. Miller, I. E. Wachs and S. G. Podkolzin, *J. Phys. Chem. C*, 2019, **123**, 22281–22292.